Inorganic Chemistry
Article
pubs.acs.org/IC

# Five Coordinate M(II)-Diphenolate [M = Zn(II), Ni(II), and Cu(II)] Schiff Base Complexes Exhibiting Metal- and Ligand-Based Redox Chemistry

Mark Franks, Anastasia Gadzhieva, Laura Ghandhi, David Murrell, Alexander J. Blake, E. Stephen Davies, William Lewis, Fabrizio Moro, Jonathan McMaster,* and Martin Schröder*

School of Chemistry, University of Nottingham, Nottingham NG7 2RD, U.K.

*Supporting Information*

**ABSTRACT:** Five-coordinate $Zn^{II}$, $Ni^{II}$, and $Cu^{II}$ complexes containing pentadentate $N_3O_2$ Schiff base ligands $[\mathbf{1A}]^{2-}$ and $[\mathbf{1B}]^{2-}$ have been synthesized and characterized. X-ray crystallographic studies reveal five coordinate structures in which each metal ion is bound by two imine N-donors, two phenolate O-donors, and a single amine N-donor. Electron paramagnetic resonance (EPR) spectroscopic studies suggest that the $N_3O_2$ coordination spheres of [Cu(**1A**)] and [Cu(**1B**)] are retained in $CH_2Cl_2$ solution and solid-state superconducting quantum interference device (SQUID) magnetometric studies confirm that [Ni(**1A**)] and [Ni(**1B**)] adopt high spin ($S = 1$) configurations. Each complex exhibits two reversible oxidation processes between +0.05 and +0.64 V vs $[Fc]^+/[Fc]$. The products of one- and two-electron oxidations have been studied by UV/vis spectroelectrochemistry and by EPR spectroscopy which confirm that each oxidation process for the $Zn^{II}$ and $Cu^{II}$ complexes is ligand-based with sequential formation of mono- and bis-phenoxyl radical species. In contrast, the one-electron oxidation of the $Ni^{II}$ complexes generates $Ni^{III}$ products. This assignment is supported by spectroelectrochemical and EPR spectroscopic studies, density functional theory (DFT) calculations, and the single crystal X-ray structure of $[Ni(\mathbf{1A})][BF_4]$ which contains Ni in a five-coordinate distorted trigonal bipyramidal geometry.

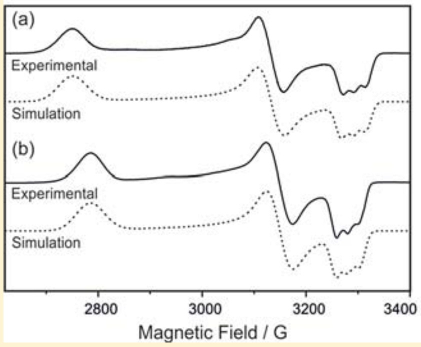

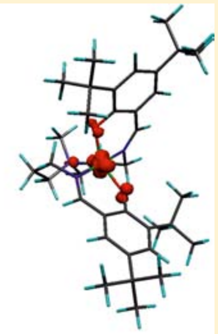

## ■ INTRODUCTION

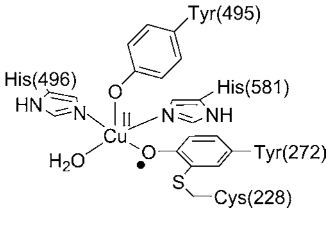

**Figure 1.** Oxidized form of the active site of GAO.[3]

The elucidation of the active site of galactose oxidase (GAO, Figure 1), which employs the $Cu^{II/I}$ and tyrosyl/tyrosinate redox couples to drive the two-electron oxidation of a broad range of primary alcohols to their corresponding aldehydes, has prompted the synthesis and characterization of low molecular weight $Cu^{II}$ complexes that contain co-ordinating redox-active phenolate groups.[1−4] The incorporation of multiple redox centers within a single molecule can lead to the formation of either a metal-ligand-radical $[M^{n+}(L^{\bullet})]$ or a high-valent metal complex on oxidation.[5] For most $Cu^{II}$-phenolate complexes, one-electron oxidation leads to a $Cu^{II}$-phenoxyl radical valence tautomer.[2,6−19] In contrast, depending on the nature of the ligand-field or the temperature of the system, the oxidation of $Ni^{II}$-phenolate complexes leads to the generation of $Ni^{III}$-phenolate or $Ni^{II}$-phenoxyl radical complexes. This behavior is a consequence of the similarity of energies for ligand-based and Ni-based redox-active orbitals in $Ni^{II}$ complexes.[20] In addition, the nature of the oxidation processes for four-coordinate $Ni^{II}$-phenolate complexes can exhibit solvent dependency, with oxidation in non-coordinating solvents leading to the formation of a predominantly ligand-based singly-occupied molecular orbital (SOMO).[20−25] The axial binding of solvent-derived pyridine to the Ni center in the oxidized species has been suggested to lead to the formation of pseudo-octahedral $Ni^{III}$-phenolate species possessing essentially metal-based SOMOs.[5,22,24,26−34] Thus, $Ni^{II}$-bisphenolate complexes that possess octahedral coordination spheres demonstrate a subtle balance between the generation on oxidation of either a high-spin $Ni^{II}$ center coordinated to a phenoxyl radical or a $Ni^{III}$ species coordinated by a phenolate ligand.[24,35−37] While the number of reported four and six coordinate $Ni^{II}$-phenolate complexes has increased steadily over recent years, the redox

**Received:** August 6, 2012
**Published:** January 8, 2013

properties of five-coordinate Ni-phenolate complexes has been little explored. These complexes possess an unsaturated coordination sphere and thus may offer further promise toward the development of novel catalytic systems. Therefore, we have investigated the chemistry of the potentially pentadentate ($N_3O_2$) Schiff base diphenolate ligands, **$H_2$1A** and **$H_2$1B** (Figure 2), which offer a route to the synthesis of five-coordinate transition metal complexes which incorporate coordinating phenolate groups. Herein we report the synthesis and structural, spectroscopic, and electrochemical characterizations of a range of pentadentate $Zn^{II}$, $Ni^{II}$, and $Cu^{II}$ complexes of **$H_2$1A** and **$H_2$1B** (Figure 2) to provide insight into their potential as new phenoxyl radical transition metal catalysts.

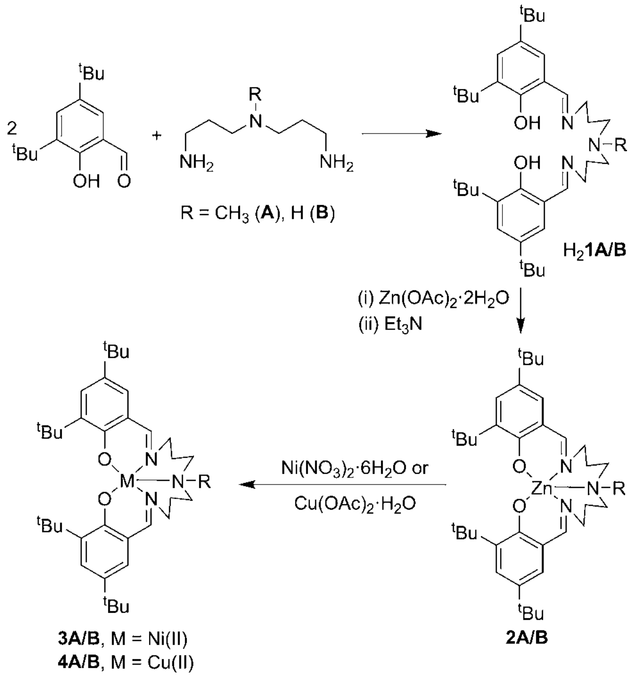

**Figure 2.** Syntheses of the pentadentate ($N_3O_2$) Schiff base diphenolate pro-ligands **$H_2$1A** and **$H_2$1B** and their corresponding $Zn^{II}$, $Ni^{II}$, and $Cu^{II}$ complexes, **2A/B**, **3A/B**, and **4A/B**, respectively.

## ■ EXPERIMENTAL SECTION

**Physical Methods.** All reagents purchased from the suppliers (including Aldrich, Acros, Lancaster, and Fluka) were used as received. $N_2$ and Ar were obtained as high-purity gases from BOC gases. Unless otherwise stated all manipulations, reactions and transfers of samples were conducted under pure Ar or $N_2$ atmospheres using standard Schlenk techniques. All solvents were predried where required; $CH_2Cl_2$ was distilled under $N_2$ over $CaH_2$, MeOH was distilled under $N_2$ over $Mg/I_2$. These solvents were stored under Ar or $N_2$ in Young's ampules.

Elemental analyses were carried out by the Microanalysis Service at the London Metropolitan University (Carlo Erba CE1108 Elemental Analyzer) and metal analyses were measured by ICP-OES using a Perkin-Elmer Optima 2000DV spectrometer (see Supporting Information for full details). Attenuated total internal reflection (ATR) solid-state infrared spectra were recorded on a Bruker Tensor 27 spectrometer. NMR spectra were recorded on a JEOL EX270, Bruker DPX 300, DPX 400 or AV 400 spectrometer. Mass spectrometric data were recorded by the Mass Spectrometry Service at the University of Nottingham using a Bruker Daltonics microTOF Electrospray Mass Spectrometer. X-band electron paramagnetic resonance (EPR) spectra were recorded on a Bruker EMX spectrometer. The simulations of EPR spectra were performed using the Bruker WINEPR SimFonia package. Magnetic measurements were obtained on samples wrapped as pellets within Teflon (possessing a negligible diamagnetic contribution) using a Quantum Design MPMS-XL5 SQUID magnetometer at the University of Nottingham. Direct current (DC) magnetic susceptibility measurements were performed from 1.8 to 300 K in an applied field of 1000 Oe for temperatures lower than 50 K and 10000 Oe for temperatures higher than 50 K.

Cyclic voltammetric measurements were made using an Eco Chemie Autolab PGSTAT20 potentiostat and performed in a single-compartment cell using a three-electrode system consisting of a glassy carbon working electrode, a Pt wire secondary electrode, and a saturated calomel reference electrode (SCE). Experiments were carried out at 293 K, unless stated otherwise, in $CH_2Cl_2$ containing 1 mM of test sample and 0.4 M $[N^nBu_4][BF_4]$ as supporting electrolyte under an atmosphere of Ar. All cyclic voltammograms were recorded at a series of scan-rates ($\nu$) (typically $\nu$ = 0.02–0.3 V $s^{-1}$), and the potentials of these measurements were referenced to the $[Fc]^+/[Fc]$ couple by internal calibration. Where necessary, the $[FeCp^*_2]^+/[FeCp^*_2]$ couple was used as the internal standard to avoid overlapping redox couples, and the $[FeCp^*_2]^+/[FeCp^*_2]$ couple was referenced to the $[Fc]^+/[Fc]$ couple by an independent calibration.

Coulometric measurements were performed in a two-compartment H-cell at 253 K in $CH_2Cl_2$ containing 0.4 M $[N^nBu_4][BF_4]$. The cell comprised a Pt/Rh gauze basket working electrode that was separated from the Pt/Rh gauze secondary electrode by a glass frit. The SCE reference electrode was sited at the center of the working electrode. The working electrode compartment was fitted with a magnetic stirrer bar, and the test solution was stirred rapidly during electrolysis.

All UV/vis spectra were recorded on a Perkin-Elmer Lambda 16 spectrometer in an optically transparent electrochemical (OTE) cell. Potentials at the working electrode were controlled by a Sycopel Scientific Ltd DD10 M potentiostat. The OTE cell consisted of a modified quartz cuvette (path length 0.05 cm) fitted with an optically transparent Pt/Rh gauze working electrode, a Pt wire secondary electrode in a fritted PTFE sleeve, and an SCE reference electrode. Both reference and secondary electrodes were connected to the cell via salt bridge tubes. The experimental temperature of 243 K was controlled by flowing a stream of cooled $N_2$ gas over the cell surface.

**X-ray Crystallography.** The unit cell, data collection and refinement parameters for **2A**, **2B**·$0.25CH_2Cl_2$, **3A**·$0.5CH_2Cl_2$, **3B**·$0.5CH_2Cl_2$, **4A**, **4B**·$0.25CH_3OH$, and [**3A**]$[BF_4]$ are presented in Supporting Information, Table S1. Diffraction data were collected using $\omega$-scans on either a Bruker SMART 1000 diffractometer, a Bruker SMART APEX CCD diffractometer using graphite-monochromated Mo $K\alpha$ radiation from a sealed X-ray tube source, or an Agilent SuperNova CCD diffractometer equipped with a Cu-$K\alpha$ micro-focus sealed tube X-ray source. Experimental temperatures were regulated using an Oxford Cryosystems open-flow nitrogen cryostat. Empirical absorption corrections were applied using SADABS.[38] Structures were solved by direct methods using SHELXS97[38] or SIR92(3)[39] and refined against $F^2$ using SHELXL97.[38] Unless otherwise stated, all non-H atoms were refined with anisotropic atomic displacement parameters, while the hydrogen atoms were placed in geometrically calculated positions. All CIFs were checked using enCIFer[40] and checkCIF.[41]

**Density Functional Theory (DFT) Calculations.** Gas phase geometry optimizations were performed for models of **3A** and [**3A**]$^+$ using coordinates derived from the single crystal X-ray structures of **3A** and [**3A**]$[BF_4]$, respectively. No constraints were imposed on the structure during the geometry optimizations. The calculations were performed using the Amsterdam Density Functional (ADF) suite version 2010.01.[42,43] The DFT geometry optimizations employed Slater type orbital (STO) triple-$\zeta$-plus polarization basis sets from the ZORA/TZP database of the ADF suite. The frozen core approximation (up to and including 3p for Ni, and 1s for C, N and O) was employed. Scalar relativistic approaches were used within the ZORA Hamiltonian for the inclusion of relativistic effects and the local density approximation (LDA) with the correlation potential due to

Vosko et al.[44] was used in all of the calculations. Gradient corrections were performed using the functionals of Becke[45] and Perdew.[46] The program MOLEKEL[47] was used to prepare the three-dimensional plot of the spin density.

**Synthesis of $H_21A$.** A solution of 3,3′-diamino-*N*-methyldipropylamine (0.15 g, 1.00 mmol) in MeOH (10 mL) was added dropwise to a stirred solution of 3,5-di-*tert*-butyl-2-hydroxybenzaldehyde (0.47 g, 2.00 mmol) in MeOH (10 mL). The reaction mixture was stirred at room temperature for 2 h before removal of the solvent in vacuo to leave $\mathbf{H_21A}$ as viscous yellow oil (0.54 g, 94%). $^1$H NMR (300 MHz, $CDCl_3$, 298K): $\delta_H$ 13.93 (2H, s, OH), 8.37 (2H, s, *H*C═N), 7.38 (2H, s, Ar*H*), 7.08 (2H, s, Ar*H*), 3.63 (4H, t, C*H*$_2$), 2.46 (4H, t, C*H*$_2$), 2.25 (3H, s, N*Me*), 1.88 (4H, m, C*H*$_2$), 1.46 (18H, s, C(C*H*$_3$)$_3$), 1.32 (18H, s, C(C*H*$_3$)$_3$). $^{13}$C NMR (75.5 MHz, $CDCl_3$, 298 K): $\delta_C$ 165.9 (*C*═N), 158.2 (Ar*C*), 139.9 (Ar*C*), 136.7 (Ar*C*), 126.7 (Ar*C*), 125.7 (Ar*C*), 117.9 (Ar*C*), 57.5 ($CH_3N$), 55.3 ($CH_2NH$), 42.1 ($CH_2$), 35.0 ($C(CH_3)_3$), 34.2 ($C(CH_3)_3$), 31.5 ($C(CH_3)_3$), 29.4 ($C(CH_3)_3$), 28.6 ($CH_2$). ESI-MS *m*/*z* (%): 578.46 (M$^+$ + H).

**Synthesis of $H_21B$.** The same procedure was adopted for the synthesis of $\mathbf{H_21B}$ as for $\mathbf{H_21A}$. Using bis(3-aminopropyl)amine (0.15 g, 1.1 mmol) in place of 3,3′-diamino-*N*-methyldipropylamine gave $\mathbf{H_21B}$ (0.59 g, 95%) $^1$H NMR (300 MHz, $CDCl_3$, 298 K): $\delta_H$ 13.83 (2H, s, OH), 8.34 (2H, s, *H*C═N), 7.36 (2H, d, Ar*H*), 7.25 (1H, s, N*H*), 7.06 (2H, d, Ar*H*), 3.62 (4H, t, C*H*$_2$), 2.71 (4H, m, C*H*$_2$), 1.87 (4H, m, C*H*$_2$), 1.42 (18H, s, C(C*H*$_3$)$_3$), 1.28 (18H, s, C(C*H*$_3$)$_3$). $^{13}$C NMR (67.9 MHz, $CDCl_3$, 298K): $\delta_C$ 166.1 (*C*═N), 158.2 (Ar*C*), 140.0 (Ar*C*), 136.7 (Ar*C*), 126.9 (Ar*C*), 125.8 (Ar*C*), 117.9 (Ar*C*), 57.6 ($CH_2N$), 47.8 ($CH_2NH$), 35.1 ($C(CH_3)_3$), 34.2 ($C(CH_3)_3$), 31.6 ($C(CH_3)_3$), 31.3 ($CH_2$), 29.5 ($C(CH_3)_3$). ESI-MS *m*/*z* (%): 564.45 (M$^+$ + H).

**Synthesis of 2A.** $Zn(OAc)_2{\cdot}2H_2O$ (0.11 g, 0.59 mmol) in MeOH (3 mL) was added dropwise to a stirred solution of $\mathbf{H_21A}$ (0.34 g, 0.59 mmol) in $CH_2Cl_2$ (20 mL). The mixture was stirred for 5 min before a solution of $Et_3N$ (0.09 mL, 0.59 mmol) in MeOH (2 mL) was added. The resulting solution was stirred for 2 h, and the volume of the solvent was reduced to 5 mL by evaporation under vacuo. The solution was cooled to −20 °C for 12 h, and the crude product collected by filtration, dissolved in $CH_2Cl_2$, and crystallized by layering hexane onto the solution. **2A** was isolated as a pale green crystalline solid (0.33 g, 87%). Anal. Calc. for $ZnC_{37}H_{57}N_3O_2$: C 69.30, H 8.96, N 6.55. Found: C 69.36, H 8.87, N 6.58. $^1$H NMR (400 MHz, $CDCl_3$, 298K): $\delta_H$ 8.11 (2H, s, N═C*H*), 7.33 (2H, d, Ar*H*), 6.91 (2H, d, Ar*H*), 4.61−4.66 (2H, m, N−C*H*$_2$), 3.41−3.46 (2H, m, N−C*H*$_2$), 2.73 (4H, m, C*H*$_2$), 2.31 (3H, s, C*H*$_3$), 2.05 (2H, m, C*H*$_2$), 1.96 (2H, m, C*H*$_2$), 1.42 (18H, s, C(C*H*$_3$)$_3$), 1.31 (18H, s, C(C*H*$_3$)$_3$). $^{13}$C NMR (100.6 MHz, $CDCl_3$, 298K): $\delta_C$ 169.4 (N=CH), 167.7 (ArC), 140.4 (ArC), 133.1 (ArC), 128.2 (ArC), 127.7 (ArC), 117.5 (ArC), 58.3 ($CH_2$), 38.5 ($CH_3$), 35.3 ($C(CH_3)_3$), 33.7 ($C(CH_3)_3$), 31.5 ($C(CH_3)_3$), 29.4 ($C(CH_3)_3$). ESI-MS *m*/*z* (%): 640.38 (M$^+$ + H).

**Synthesis of 2B.** The same procedure was adopted for the synthesis of **2B** as for **2A**. Using $\mathbf{H_21B}$ (0.33 g, 0.59 mmol) in place of $\mathbf{H_21A}$ gave **2B** (0.32 g, 87%). Anal. Calc. for $ZnC_{36}H_{55}N_3O_2$: C 68.94, H 8.84, N 6.70. Found: C 69.00, H 8.77, N 6.66. $^1$H NMR (270 MHz, $CDCl_3$, 298K): $\delta_H$ 8.12 (2H, s, N═C*H*), 7.32 (2H, s, Ar*H*), 6.90 (2H, s, Ar*H*), 4.52 (2H, m, N−C*H*$_2$), 3.38 (2H, m, N−C*H*$_2$), 2.94 (2H, m, C*H*$_2$), 2.74 (2H, m, C*H*$_2$), 2.07 (2H, m, C*H*$_2$), 1.85 (2H, m, C*H*$_2$), 1.41 (18H, s, C(C*H*$_3$)$_3$), 1.30 (18H, s, C(C*H*$_3$)$_3$). $^{13}$C NMR (67.9 MHz, $CDCl_3$, 298K): $\delta_C$ 169.1 (N=CH), 168.4 (ArC), 140.6 (ArC), 133.4 (ArC), 128.6 (ArC), 127.9 (ArC), 117.8 (ArC), 58.5 ($CH_2$), 49.2 ($CH_2$), 42.2 ($CH_2$), 35.5 ($C(CH_3)_3$), 33.8 ($C(CH_3)_3$), 31.6 ($C(CH_3)_3$), 29.6 ($C(CH_3)_3$). IR/cm$^{-1}$ (KBr): 2956 (s), 2864 (s), 1629 (s) 1437 (s), 1258 (m). ESI-MS *m*/*z* (%): 626.5 (M$^+$ + H).

**Synthesis of 3A.** $Ni(NO_3)_2{\cdot}6H_2O$ (0.05 g, 0.16 mmol) in MeOH (3 mL) was added dropwise to a stirred solution of **2A** (0.10 g, 0.16 mmol) in $CH_2Cl_2$ (25 mL). The mixture was stirred for 2 h, and the solvent volume was reduced to about 5 mL under vacuo. The addition of excess MeOH to this solution precipitated the crude material. Recrystallization by layering MeOH onto a solution of the complex in $CH_2Cl_2$ gave pure **3A** as a dark green crystalline solid (0.09 g, 91%). Anal. Calc. for $NiC_{37}H_{57}N_3O_2$: C 70.03, H 9.05, N 6.62, Ni 9.2, Zn 0.0%. Found: C 70.06, H 9.11, N 6.53, Ni 9.4, Zn 0.0%. IR/cm$^{-1}$ (KBr): 2951 (s), 2859 (m), 1627 (s), 1528 (m), 1435 (s), 1410 (m), 1324 (s), 1163 (m), 740 (m). ESI-MS *m*/*z* (%): 634.38 (M$^+$ + H).

**Synthesis of 3B.** The same procedure was adopted for the synthesis of **3B** as for **3A**. Using **2B** (0.10 g, 0.18 mmol) in place of **2A** gave **3B** (0.10 g, 90%). Anal. Calc. for $NiC_{36}H_{55}N_3O_2$: C 69.68, H 8.93, N 6.77, Ni 9.5, Zn 0.0%. Found: C 69.75, H 8.96, N 6.70, Ni 9.0, Zn 0.0%. IR/cm$^{-1}$ (KBr): 2954 (s), 2863 (m), 1631 (s), 1580 (m), 1453 (s), 1234 (m), 727 (w). FAB-MS *m*/*z* (%): 620.3 (M$^+$ + H).

**Synthesis of [3A][BF$_4$].** $AgBF_4$ (0.04 g, 0.16 mmol) was added to a stirred solution of **3A** (0.10 g, 0.16 mmol) in $CH_2Cl_2$ (10 mL). After stirring for 2 min the solution was filtered and evaporated to dryness in vacuo. The dark brown solid was washed three times with pentane and dried yielding [**3A**][BF$_4$] as a dark brown crystalline solid (0.09 g, 85%). Anal. Calc. for $NiC_{37}H_{57}N_3O_2BF_4$: C 61.60, H 7.96, N 5.83, Ni 8.1, Zn 0.0%. Found: C 61.49, H 7.91, N 5.73, Ni 8.5, Zn 0.0%. ESI-MS *m*/*z* (%): 634.38 (M$^+$ + H).

**Synthesis of 4A.** A solution of $Cu(OAc)_2.H_2O$ (0.03 g, 0.16 mmol) in MeOH (3 mL) was added dropwise to a stirred solution of **2A** (0.10 g, 0.16 mmol) in $CH_2Cl_2$ (25 mL). The reaction mixture was stirred for 2 h before the solvent volume was reduced to about 5 mL under vacuo. The addition of excess MeOH precipitated the crude product. Crystallization by layering MeOH onto a solution of the crude complex in $CH_2Cl_2$ solution gave **4A** as a pure, dark green crystalline solid (0.09 g, 92%). Anal. Calc. for $CuC_{37}H_{57}N_3O_2$: C 69.50, H 8.99, N 6.57, Cu 9.9, Zn 0.0%. Found: C 69.58, H 9.08, N 6.54, Cu 9.3, Zn 0.0%. IR/cm$^{-1}$ (KBr): 2952 (s), 2863 (m), 1630 (s), 1528 (m), 1463 (m), 1437 (s), 1411 (m), 1326 (s), 1160 (m), 748 (m). ESI-MS *m*/*z* (%): 639.38 (M$^+$ + H).

**Synthesis of 4B.** The same procedure was adopted for the synthesis of **4B** as for **4A**. Using **2B** (0.10 g, 0.18 mmol) in place of **2A** gave **4B** (0.10 g, 92%). Anal. Calc. for $CuC_{36}H_{55}N_3O_2$: C 69.14, H 8.86, N 6.72, Cu 10.2, Zn 0.0%. Found: C 69.03, H 8.77, N 6.64, Cu 9.4, Zn 0.0%. IR/cm$^{-1}$ (KBr): 2950 (s), 2853 (m), 1629 (s), 1530 (m), 1456 (m), 1437 (s), 1411 (m), 1324 (s), 1257 (s), 1167 (m), 741 (m). ESI-MS *m*/*z* (%): 625.36 (M$^+$ + H).

## ■ RESULTS AND DISCUSSION

**Synthesis of $H_21A$ and $H_21B$.** Treatment of a solution of 3,5-di-*tert*-butyl-2-hydroxybenzaldehyde in MeOH with 3,3′-diamino-*N*-methyldipropylamine or bis(3-aminopropyl)amine affords the desired Schiff-base phenol pro-ligands $\mathbf{H_21A}$ and $\mathbf{H_21B}$, respectively, in high yield (ca. 95%). The formation of each compound was confirmed by $^1$H and $^{13}$C NMR spectroscopies and mass spectrometry (ES$^+$).

**Synthesis and Structural Characterization of 2A and 2B.** The reaction of $\mathbf{H_21A}$ and $\mathbf{H_21B}$ with $Zn(OAc)_2{\cdot}2H_2O$ yielded the complexes **2A** and **2B**, respectively. The solid state structures of **2A** and **2B**·0.25($CH_2Cl_2$) (Figure 3, Table 1) have been determined by X-ray crystallography. In each case, the monomeric five-coordinate Zn$^{II}$ center is supported by a $N_3O_2$ ligand set consisting of two phenolate O-donors, two imine N-donors and either a secondary or tertiary amine N-donor, which are located in the *N*-methyldipropylamine and dipropylamine bridges which link the phenol groups in **2A** and **2B**, respectively. The Zn(1)-O(phenolate) (ca. 1.98 Å) and Zn(1)-N(imine) (ca. 2.08 Å) bond distances (Table 1) are comparable to those of (1,2-cyclohexanediamino-*N*,*N*′-bis-(3,5-di-*tert*-butylsalicylidene))pyridine zinc(II)[48] and 2,2′-(methyl-4-azaheptane-1,7-diylbis(nitrilomethylidyne))-diphenolato zinc(II) which also contains a Zn$^{II}$ metal center in an $N_3O_2$ coordination sphere (ca. 1.96 Å and 2.07 Å, respectively).[49] The Zn(1)−N(3) interaction is the longest of the three Zn(1)−N bond distances (ca. 2.16 Å) in the complex. This is consistent with the relative donor strength of N(imine) and N(amine) centers and with the Zn−N(amine) bond

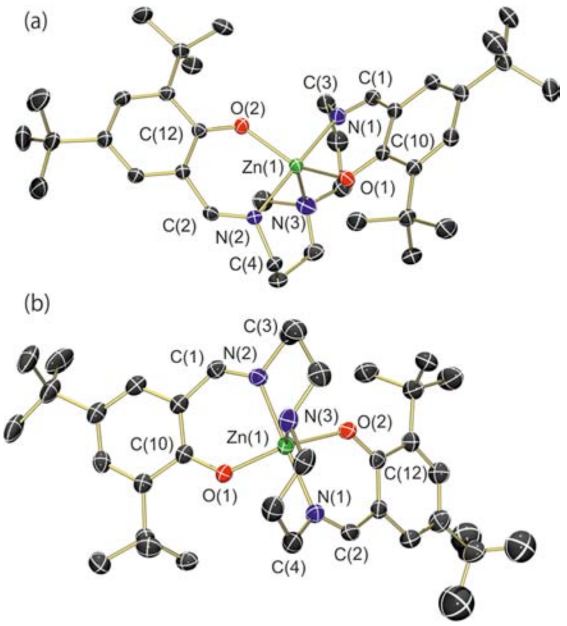

**Figure 3.** Views of the molecular structures of (a) **2A** and (b) **2B** with displacement ellipsoids at the 50% probability level and H atoms omitted for clarity.

distance found within the five coordinate Zn$^{II}$ $N_3O_2$ complex of *N,N*-bis((2-hydroxy-5-methylphenyl)-phenylmethylene)-4-azaheptane-1,7-diamine (ca. 2.16 Å).[49,50] The bond angles about each Zn$^{II}$ center (Table 1) show that **2A** and **2B** adopt distorted trigonal bipyramidal coordination geometries [$\tau$ = 0.68 (**2A**) and 0.72 (**2B**); for ideal square-pyramidal geometry $\tau$ = 0 and for ideal trigonal bipyramidal $\tau$ = 1][51] in which the equatorial plane is composed of the two O(phenolate) donors and a single N(amine) donor, the remaining two N(imine) donors occupy the axial positions. Deviations from the expected 180°, 120°, and 90° bond angles for a regular trigonal bipyramidal geometry are expected and observed as a result of the N(1)−Zn(1)−N(3), N(1)−Zn(1)−O(1), and N(2)−Zn(1)−O(2) bite angles which are enforced by the chelating nature of the ligand frameworks in geometry **2A** and **2B.**[51]

**Synthesis and Structural Characterization of 3A, 3B, 4A, and 4B.** The syntheses of **3A**, **3B**, **4A**, and **4B** can be achieved by the direct reaction of **$H_2$1A** and **$H_2$1B** with the appropriate metal salt. However, these reactions did not proceed to completion and caused problems in purification. Transmetalation of **2A** or **2B** via addition of a stoichiometric quantity of $Ni(NO_3)_2 \cdot 6H_2O$ (for **3A** and **3B**) or $Cu(OAc)_2 \cdot H_2O$ (for **4A** and **4B**) was found to be an effective alternative route to yield pure products after a single recrystallization step. We confirmed the metal content of **3A**, **3B**, **4A**, and **4B** by ICP-OES analysis. The single crystal X-ray structures of **3A**$\cdot 0.5CH_2Cl_2$, **3B**$\cdot 0.5CH_2Cl_2$, **4A**, and **4B**·0.25MeOH have been determined (Supporting Information, Table S1, Table 1, and Figure 4), and in each case, the metal center is supported within an $N_3O_2$-coordination sphere in a distorted square-based pyramidal coordination geometry ($\tau$ = 0.47, 0.47, 0.37, and 0.42 for **3A**, **3B**, **4A** and **4B**, respectively) where the equatorial plane is composed of two phenolate O-donors and two imine N-donors arranged in a trans configuration. The non-imine N-donor associated with the dipropylamine or N-methyldipropylamine bridges that link the phenolate groups occupy the axial position (Figure 4). Distortions away from the 180° and 90° bond angles for a regular square-based pyramidal geometry in **3A**, **3B**, **4A**, and **4B** are a consequence of the strain induced upon the equatorial donors by the incorporation of dipropylamine and *N*-methydipropylamine bridges.

**Table 1. Selected Bond Distances (Å) and Angles (deg) with s.u.'s for 2A, 2B, 3A, 3B, 4A, 4B, and [3A][$BF_4$], where M = Zn(2A/B), Ni(3A/B), and Cu(4A/B)**[a]

| M = Zn, Ni,[a] Cu | **2A** | **2B** | **3A** | **3B** | **4A** | **4B** | [3A][$BF_4$] | model of **3A** | model of [3A]$^+$ |
|---|---|---|---|---|---|---|---|---|---|
| M(1)−N(1) | 2.0535(11) | 2.094(3) | 2.009(3) | 1.9846(14) | 1.9668(10) | 1.978(3) | 1.8916(18) | 2.018 | 1.908 |
| M(1)−N(2) | 2.0702(11) | 2.081(3) | 2.009(3) | 1.9846(14) | 1.9602(10) | 1.982(3) | 1.8943(19) | 2.019 | 1.926 |
| M(1)−N(3) | 2.1781(12) | 2.137(3) | 2.099(4) | 2.052(3) | 2.3401(11) | 2.262(3) | 2.0459(19) | 2.169 | 2.322 |
| M(1)−O(1) | 1.9814(9) | 1.964(2) | 1.996(2) | 1.9846(14) | 1.9670(8) | 1.948(2) | 1.9304(15) | 2.058 | 1.916 |
| M(1)−O(2) | 1.9907(9) | 1.978(3) | 1.996(2) | 1.9846(14) | 1.9573(9) | 1.966(2) | 1.8770(16) | 2.069 | 1.971 |
| N(1)−C(1) | 1.2795(17) | 1.278(5) | 1.291(4) | 1.283(2) | 1.2855(15) | 1.293(4) | 1.288(3) | 1.302 | 1.303 |
| N(1)−C(3) | 1.4640(16) | 1.473(5) | 1.464(4) | 1.466(3) | 1.4677(15) | 1.474(4) | 1.467(3) | 1.458 | 1.465 |
| N(2)−C(2) | 1.2791(17) | 1.284(5) | 1.291(4) | 1.283(2) | 1.2874(15) | 1.285(4) | 1.295(3) | 1.301 | 1.301 |
| N(2)−C(4) | 1.4636(17) | 1.475(5) | 1.464(4) | 1.466(3) | 1.4715(14) | 1.484(4) | 1.477(3) | 1.455 | 1.462 |
| O(1)−C(10) | 1.3073(15) | 1.302(4) | 1.301(4) | 1.304(2) | 1.3066(14) | 1.307(4) | 1.316(3) | 1.307 | 1.318 |
| O(2)−C(12) | 1.3024(16) | 1.313(5) | 1.301(4) | 1.304(2) | 1.3082(14) | 1.311(4) | 1.313(3) | 1.308 | 1.319 |
| N(1)−M(1)−N(2) | 178.54(4) | 178.48(13) | 179.09(15) | 179.38(9) | 174.75(4) | 175.63(12) | 176.54(8) | 179.4 | 179.5 |
| N(1)−M(1)−N(3) | 89.39(5) | 86.36(13) | 90.46(8) | 89.69(4) | 87.23(4) | 84.75(11) | 87.58(8) | 89.8 | 90.1 |
| N(2)−M(1)−N(3) | 89.15(5) | 92.31(13) | 90.46(8) | 89.69(4) | 87.53(4) | 90.90(11) | 91.55(8) | 90.8 | 90.5 |
| N(1)−M(1)−O(1) | 88.83(4) | 88.68(11) | 88.56(10) | 89.22(6) | 89.60(4) | 91.52(11) | 92.75(7) | 88.3 | 92.6 |
| N(2)−M(1)−O(1) | 91.78(4) | 92.56(11) | 91.21(10) | 90.93(6) | 91.83(4) | 90.10(10) | 90.72(7) | 82.0 | 87.9 |
| N(3)−M(1)−O(1) | 111.51(5) | 115.14(12) | 104.67(7) | 104.29(4) | 103.58(4) | 105.66(10) | 102.86(8) | 102.6 | 123.8 |
| N(1)−M(1)−O(2) | 92.79(4) | 91.69(11) | 91.21(10) | 90.93(6) | 90.26(4) | 90.94(10) | 85.46(7) | 92.2 | 90.6 |
| N(2)−M(1)−O(2) | 87.65(4) | 88.05(11) | 88.56(10) | 89.22(6) | 90.80(4) | 89.66(10) | 93.17(8) | 87.3 | 89.1 |
| N(3)−M(1)−O(2) | 110.58(5) | 109.56(12) | 104.67(7) | 104.29(4) | 103.80(4) | 103.97(10) | 141.68(8) | 104.7 | 95.5 |
| O(1)−M(1)−O(2) | 137.89(4) | 135.22(12) | 150.66(13) | 151.43(8) | 152.58(4) | 150.38(10) | 115.07(7) | 152.7 | 140.5 |

[a] For M = Ni, N(2) = N(1A), O(2) = O(1A), C(2) = C(1A), C(4) = C(3A), and C(12) = C(10A).

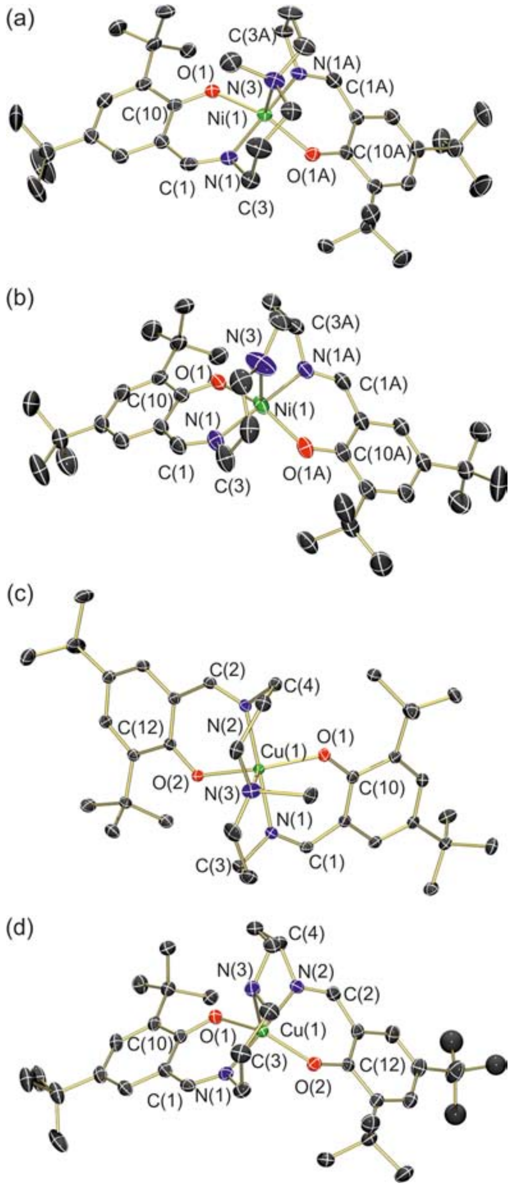

**Figure 4.** Views of the molecular structures of (a) **3A**, (b) **3B**, (c) **4A**, and (d) **4B** with displacement ellipsoids at the 50% probability level and H atoms omitted for clarity.

Selected bond lengths and angles for **3A**, **3B**, **4A**, and **4B** are presented in Table 1. The average length of the Ni(1)-O(phenolate) (ca. 1.99 Å), Ni(1)-N(imine) (ca. 2.00 Å), and Ni(1)-N(amine) (ca. 2.07 Å) bonds of **3A** and **3B** are comparable to those of [Ni(Saldipa)] [Saldipa = bis-(salicylidene-$\gamma$-iminopropyl)amine], [Ni(SalMeDPT)] [SalMeDPT = bis(salicylidene-$\gamma$-iminopropyl)methylamine] and [Ni(Me-sal)$_2$DPT] [(Me-sal)$_2$DPT = *N*,*N*-bis($\alpha$-methylsalicylidene)dipropylenetriamine)] that also contain Ni$^{II}$ centers within an N$_3$O$_2$-coordination sphere [Ni−O(phenolate) = 1.93−2.02 Å, Ni−N(imine) = 2.01−2.03 Å and Ni−N(amine) = 2.04−2.10 Å].[52−56] A comparison of the Ni(1)−N(3) bond lengths of **3A** and **3B** [2.099(4) Å and 2.052(3) Å, respectively] shows an increase of about 0.05 Å upon changing the N-donor from a secondary to a tertiary amine. This could result from steric interactions associated with the methyl group at the N(3) position within **3A** and the adjacent phenolate O(1) atom (contact distance ca. 3.21 Å). A similar trend is also apparent within the analogous Zn$^{II}$ and Cu$^{II}$ structures (**2A**, **2B**, **4A**, and **4B**, Table 1).

The average Cu(1)-O(phenolate) (ca. 1.96 Å) and Cu(1)-N(imine) (ca. 1.97 Å) bond lengths of **4A** and **4B** are comparable to those of [Cu(salenN3)] [salenN3 = 2-({[3-(methyl{3-[(2-hydroxybenzylidene)amino]propyl}-amino)-propyl]imino}methyl)phenol, ca. 1.95 Å and 1.96 Å, respectively], which also contains Cu$^{II}$ in a pentadentate N$_3$O$_2$ coordination sphere.[57] The nonimine N-donor forms the longest of the three Cu(1)-N bond distances [2.3401(11) Å and 2.262(3) Å for **4A** and **4B**, respectively], and are consistent with the Cu−N(amine) bond distance observed within 1-ethyl-4,7-bis(3-*tert*-butyl-5-methoxy-2-hydroxy-benzyl)-1,4,7-triazacyclononane copper(II) (ca. 2.36 Å).[13] A comparison of the M(1)-N(3) bond distances for M = Ni, Cu and Zn (Table 1) shows that this distance is greatest for M = Cu, consistent with weaker axial ligation associated with a Jahn−Teller distorted Cu$^{II}$ center.

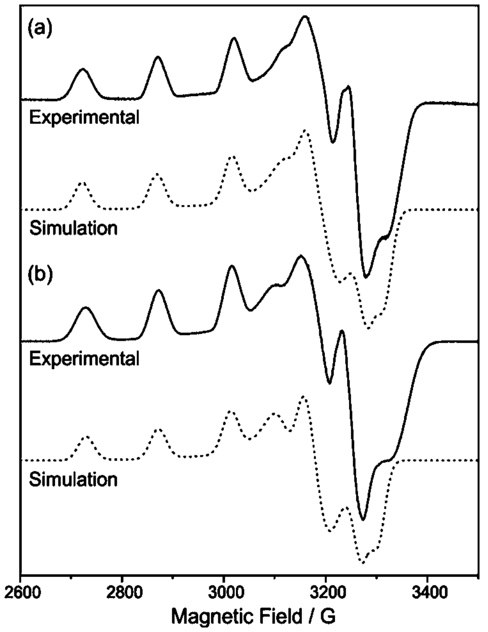

**Figure 5.** Frozen solution EPR spectra of (a) **4A** and (b) **4B** in CH$_2$Cl$_2$ containing $[\mathrm{N}^n\mathrm{Bu}_4][\mathrm{BF}_4]$ (0.4 M) at 77 K (top), simulated spectra (dotted lines).

**EPR Spectra of 4A and 4B and UV−vis spectra of 2A, 2B, 3A, 3B, 4A, and 4B.** The X-band EPR spectra of **4A** and **4B** in CH$_2$Cl$_2$ solutions containing $[\mathrm{N}^n\mathrm{Bu}_4][\mathrm{BF}_4]$ (0.4 M) at 77 K are shown in Figure 5. **4A** and **4B** possess rhombic $S = 1/2$ EPR spectra with $^{63,65}$Cu hyperfine splitting clearly resolved in the $g_{33}$ region. The spectra may be simulated with the spin Hamiltonian parameters: **4A**: $g_{11} = 2.025$, $g_{22} = 2.112$, $g_{33} = 2.255$; $A_{11}\{^{63,65}\mathrm{Cu}\} = 1$ G, $A_{22}\{^{63,65}\mathrm{Cu}\} = 5$ G, $A_{33}\{^{63,65}\mathrm{Cu}\} = 147$ G; **4B**: $g_{11} = 2.031$, $g_{22} = 2.125$, $g_{33} = 2.254$; $A_{11}\{^{63,65}\mathrm{Cu}\} = 1$ G, $A_{22}\{^{63,65}\mathrm{Cu}\} = 6$ G, $A_{33}\{^{63,65}\mathrm{Cu}\} = 142$ G. These parameters are similar to those for the five-coordinate square-based pyramidal Cu$^{II}$ complex [Cu(L$^2$H)]CH$_3$OH [L$^2$H = 1,4,7-tris(3-*tert*-butyl-5-methoxy-2-hydroxy-benzyl)1,4,7-triazacyclononane] ($g_{xx} = 2.06$, $g_{yy} = 2.05$, $g_{zz} = 2.25$; $A_{xx}\{^{63,65}\mathrm{Cu}\} = A_{yy}\{^{63,65}\mathrm{Cu}\} = 10.7$ G, $A_{zz}\{^{63,65}\mathrm{Cu}\} = 192.8$ G) and suggest that the N$_3$O$_2$ coordination spheres of **4A** and **4B** are retained in solution.[58]

The electronic spectra of **2A**, **2B**, **3A**, **3B**, **4A**, and **4B** have been recorded in $CH_2Cl_2$ solution (Table 2 and Supporting Information, Figure S1). The UV/vis absorption spectra of **2A** and **2B** are characterized by bands at about 270 and 368 nm associated with $\pi \rightarrow \pi^*$ transitions involving molecular orbitals located primarily on the phenolate chromophore.[59,60] The analogous $Ni^{II}$ complexes, **3A** and **3B**, exhibit features at about 238 and 376 nm, that are assigned to phenoxide $\pi \rightarrow \pi^*$ transitions and a ligand-to-metal charge transfer (LMCT) transition involving the phenolate donors and the $Ni^{II}$ center, respectively. These assignments are consistent with those observed in $[Ni(L^{Py})]$ [$L^{Py}$ = *N,N′,N,N′*-bis[(2-hydroxy-3,5-di-*tert*-butylbenzyl)(2-pyridylmethyl)]-ethylene diamine)] and $[Ni(L^{AmH})_2]$ [$L^{AmH}$ = 3,5-di-*tert*-butyl-*N*-(dimethylamino-ethyl)salicylideneamine)].[34,35,60] The absorption spectra of **4A** and **4B** contain bands at about 234, 309, 377, and 704−712 nm consistent with $Cu^{II}$-phenolate complexes possessing square-based pyramidal geometries including 1-ethyl-4,7-bis(3-*tert*-butyl-5-methoxy-2-hydroxy-benzyl)-1,4,7-triazacyclononane copper(II) (252, 314, 458, and 698 nm) and *N*-benzyl-*N′*,*N″*-di-*tert*-butyl-disalicyl-triaminocyclohexane copper(II) (230, 258, 326, 378, and 594 nm).[4,13] The bands at 234 and 309 nm in the electronic spectra of **4A** and **4B** are associated with phenoxide $\pi \rightarrow \pi^*$ charge transfer transitions, while the absorption at 377 nm is assigned to LMCT from the phenolate donors to the $Cu^{II}$ center. The band at about 704−712 nm is assigned to a ligand field (d → d) transition.[12,57,58,61−63]

**Table 2. UV/vis Spectra of 2A, 2B, 3A, 3B, 4A, and 4B (at 243 K) and Their One- and Two-Electron Oxidation Products (at 243 K) in an OTE Cell for Solutions of Compound (ca. 1 mM) in $CH_2Cl_2$ Containing $[N^nBu_4][BF_4]$ (0.4 M)**

| species | $\lambda_{max}$ (nm), $\varepsilon$ ($M^{-1}$ $cm^{-1}$) | isosbestic points/nm |
|---|---|---|
| **2A** | 269sh (20500); 368 (17400) | |
| $[\mathbf{2A}]^+$ | 276 (19500); 331 (7200); 376 (11900); 421sh (5300); 789 (940) | 275, 343, 393 |
| $[\mathbf{2A}]^{2+}$ | 286 (13700); 333 (10400); 380 (9900); 402 (10200); 426 (12900); 778 (1400) | |
| **2B** | 240 (37200); 271sh (15800); 368 (14000) | |
| $[\mathbf{2B}]^+$ | 277 (14900); 330 (6400); 379 (9800); 421sh (4600); 782 (790) | 275, 343, 393 |
| $[\mathbf{2B}]^{2+}$ | 235 (38800); 288 (11300); 333 (8900); 381 (7600); 406sh (7900); 424 (9400); 775 (1400) | |
| **3A** | 238 (84300); 376 (18300) | |
| $[\mathbf{3A}]^+$ | 271 (35100); 303 (37700); 388 (19200); 485 (9500); 668 (2700) | 266, 368, 377 |
| $[\mathbf{3A}]^{2+}$ | 296sh (20400); 397 (11600); 420 (14100); 491 (3200); 801 (2500) | |
| **3B** | 238 (52100); 375 (11100) | |
| $[\mathbf{3B}]^+$ | 272 (23300); 299 (23400); 387 (11400); 485 (5400); 669 (2000) | 263, 360, 380 |
| $[\mathbf{3B}]^{2+}$ | 294sh (11800); 395 (7600); 418 (8700); 487 (2500); 799 (1400) | |
| **4A** | 276sh (17600); 309 (10300); 376 (12100); 704 (270) | |
| $[\mathbf{4A}]^+$ | 280 (20800); 322 (10200); 386 (10500); 720 (1300) | 271, 293, 314, 358, 388 |
| $[\mathbf{4A}]^{2+}$ | 298 (18300); 394 (8700); 430 (9800); 494 (2400); 764 (1900) | |
| **4B** | 276sh (16700); 309 (9700); 377 (12600); 712 (360) | |
| $[\mathbf{4B}]^+$ | 280 (20800); 315 (9900); 388 (11000); 722 (1100) | 272, 301, 309, 357, 389 |
| $[\mathbf{4B}]^{2+}$ | 295 (18600); 391 (8800); 430 (10100); 492 (2300); 765 (1900) | |

**Magnetic Properties of 3A and 3B.** The $Ni^{II}$ complexes, **3A** and **3B**, exhibit broad resonances between 0−12 ppm in the $^1H$ NMR spectrum. Superconducting quantum interference device (SQUID) magnetometry (2−300 K) confirms that **3A** and **3B** are paramagnetic ($d^8$, $S = 1$) high-spin $Ni^{II}$ species with $\mu_{eff} = 2.97\ \mu_B$ and $3.05\ \mu_B$, for **3A** and **3B**, respectively at 300 K (see Supporting Information, Figure S2). **3A** and **3B** are EPR silent at X-band frequencies which is not unexpected since high-spin $Ni^{II}$ complexes usually exhibit zero-field splitting parameters larger than the X-band quantum (0.3 $cm^{-1}$).[64−66]

**Cyclic Voltammetry of 2A, 2B, 3A, 3B, 4A, and 4B.** The cyclic voltammograms of **2A** and **2B** (Figure 6a) in $CH_2Cl_2$ at 293 K display two electrochemically-reversible, single-electron oxidation processes [for **2A**: $E_{1/2}$ = +0.30 and +0.54 V vs $[Fc]^+/[Fc]$; for **2B**: $E_{1/2}$ = +0.29 and +0.50 V vs $[Fc]^+/[Fc]$, Table 3]. Given the expected redox inactivity of $Zn^{II}$ over the experimental potential range (−2.20 to +1.20 V vs $[Fc]^+/[Fc]$), these redox processes are attributed to the successive one-electron oxidation of each coordinated phenolate ligand forming mono- and bis-phenoxyl radical species. The difference

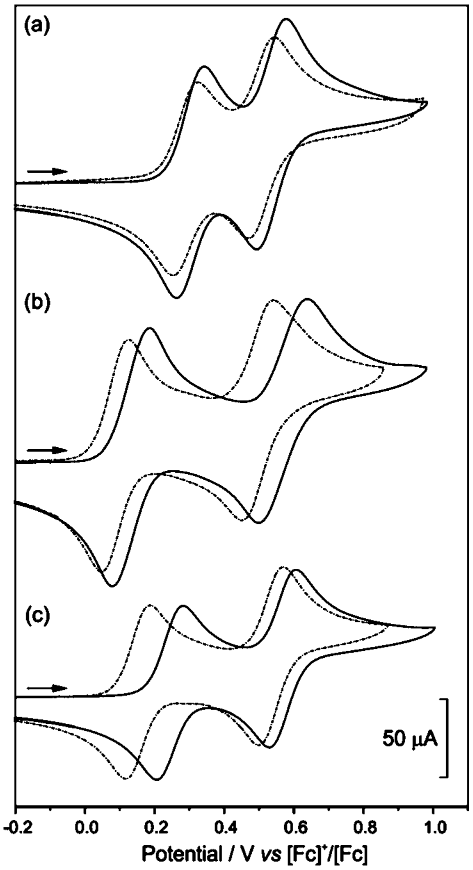

**Figure 6.** Cyclic voltammograms of (a) **2A** (solid line) and **2B** (dot-dashed line) and (b) **3A** (solid line) and **3B** (dot-dashed line) and (c) **4A** (solid line) and **4B** (dot-dashed line). Data were recorded at a scan rate of 100 mV $s^{-1}$ using a glassy carbon working electrode with about 1 mM solution in $CH_2Cl_2$ at 293 K containing $[N^nBu_4][BF_4]$ (0.4 M). The potential is expressed relative to the $[Fc]^+/[Fc]$ couple recorded under the same conditions.

**Table 3. Oxidation Potentials for 2A, 2B, 3A, 3B, 4A, and 4B at a Scan Rate of 0.1 V s$^{-1}$**

| complex | $^{1}E_{1/2}$ vs Fc$^+$/Fc ($\Delta E$) /V | $^{2}E_{1/2}$ vs Fc$^+$/Fc ($\Delta E$) /V | $\Delta E_{Fc+/Fc}$ /V |
|---|---|---|---|
| **2A** | 0.30 (0.08) | 0.54 (0.09) | 0.08 |
| **2B** | 0.29 (0.07) | 0.50 (0.08) | 0.08 |
| **3A** | 0.13 (0.10) | 0.57 (0.14) | 0.07 |
| **3B** | 0.09 (0.07) | 0.50 (0.09) | 0.07 |
| **4A** | 0.24 (0.07) | 0.57 (0.08) | 0.07 |
| **4B** | 0.15 (0.08) | 0.54 (0.08) | 0.07 |

in potential between the first and second oxidation processes of **2A** and **2B** (+0.24 and +0.21 V for **2A** and **2B**, respectively) indicates that there is communication between the two phenolate moieties consistent with the formation of a phenoxyl radical that is delocalized across the molecular framework in the one-electron oxidized form.[34,67]

The cyclic voltammograms of **3A** and **3B** in $CH_2Cl_2$ at 293 K each exhibit two, one-electron oxidation couples that demonstrate quasi-reversible electrochemical behavior in the range between +0.05 and +0.64 V vs [Fc]$^+$/[Fc] (Table 3, Figure 6b). These potentials are intermediate between those reported previously for four-coordinate [Ni($^{Me}$L)] [$^{Me}$L = *N,N*′-bis(3,5-di-*tert*-butyl-salicylaldene)-4,5-dimethyl-1,2-phenylenediamine; $E_{1/2}$ = +0.49 V and +0.78 V vs Fc$^+$/Fc][28] and six-coordinate [Ni(L$^{tBuI}$)] [L$^{tBuI}$ = 2-hydroxy-4,6-di-*tert*-butylbenzyl-2-(pyridylmethyl)imine); $E_{1/2}$ = −0.01 V and +0.32 V vs Fc$^+$/Fc].[24] Thus, the incorporation of a fifth donor shifts the potential of each redox process cathodically relative to those in related four-coordinate Ni$^{II}$ complexes.

Complexes **4A** and **4B** each exhibit two electrochemically-reversible, one-electron oxidation processes [**4A**: $E_{1/2}$ = +0.24 and +0.57 V vs [Fc]$^+$/[Fc], and **4B**: $E_{1/2}$ = +0.15 and +0.54 V vs [Fc]$^+$/[Fc], Table 3, Figure 6c]. An additional irreversible reduction process is observed at about −1.90 V vs [Fc]$^+$/[Fc] which is likely to involve reduction of the Cu$^{II}$ center to Cu$^{I}$. This process was not investigated further. The potentials of the first and second oxidation processes for **4A** and **4B** are similar to those reported for [Cu($^t$BuL$_O{}^1$)$_2$] [H$^t$BuL$_O{}^1$ = [2′-(4′,6′-di-*tert*-butylhydroxyphenyl)]-4,5-diphenylimidazole and [Cu($^t$BuL$_O{}^2$)$_2$] [H$^t$BuL$_O{}^2$ = 2-[2′-(4′,6′-di-*tert*-butylhydroxyphenyl)]-4,5-bis(*p*-methoxyphenyl)imidazole, which exhibit two reversible ligand-based oxidation processes [for [Cu($^t$BuL$_O{}^1$)$_2$] $E_{1/2}$ = +0.16 and +0.50 V vs [Fc]$^+$/[Fc]; for [Cu($^t$BuL$_O{}^2$)$_2$] $E_{1/2}$ = +0.11 and +0.44 V vs [Fc]$^+$/[Fc]] associated with the formation of [Cu($^R$L)($^R$L$^\bullet$)]$^+$ and [Cu($^R$L$^\bullet$)$_2$]$^{2+}$, respectively.[7−10]

The first oxidation process for **4B** occurs at a potential that is about 100 mV more cathodic than the corresponding process for **4A**. A comparison of the solid state structures of **4A** and **4B** [Figure 4 (c) and (d), Table 1] shows that the Cu(1)−N(3) bond distance decreases by about 0.08 Å on going from **4A** to **4B**. Thus, there appears to be a correlation between the more cathodic oxidation redox potential exhibited by **4B** and a shorter Cu(1)−N(3) distance in the solid state structure that could result in an increased electron density at the metal center. A similar trend is also apparent for the analogous Zn$^{II}$ (**2A** and **2B**) and Ni$^{II}$ (**3A** and **3B**) complexes. However, we note that differences in basicity of the amine donor atom N(3) in **2A**/**B**, **3A**/**B**, and **4A**/**B** in solution, and the consequent differences in the reduction potential, could result from the different environments of these centers, notably the extent of hydrogen bonding interactions involving N(3) and trace water in the electrochemical solvent which could be mediated by steric and/or electronic effects. A change at the metal center also has a significant effect on the potential of the first redox couple; thus,

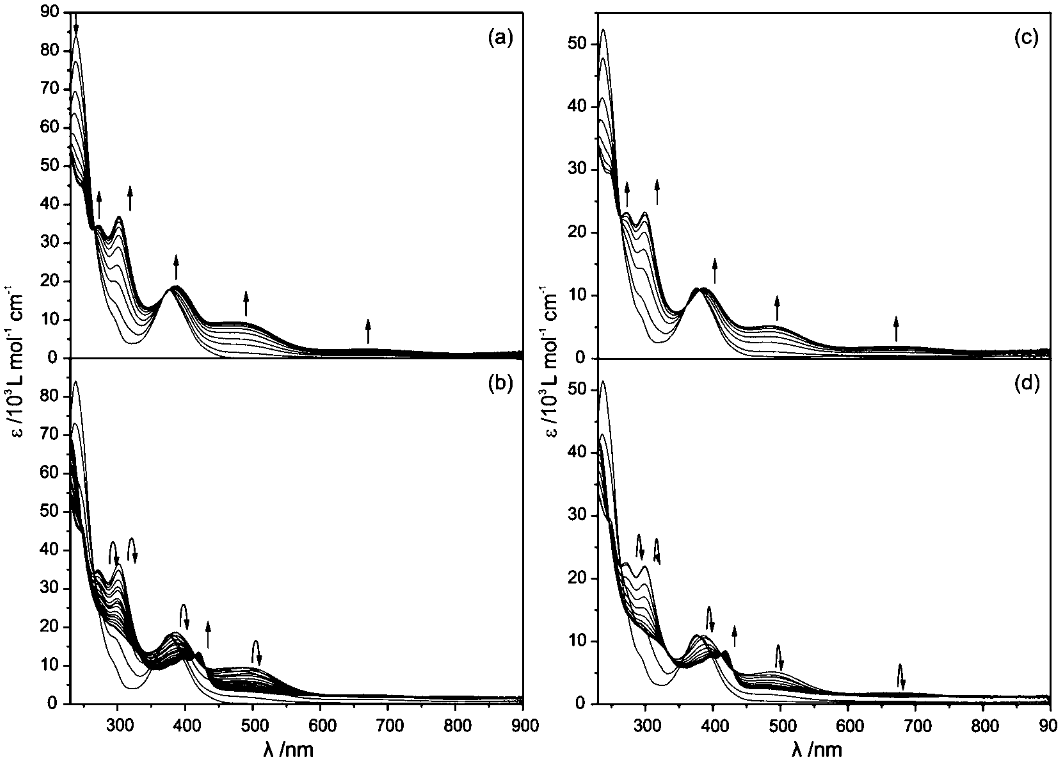

**Figure 7.** Sequential UV/vis spectra taken during (a) one- and (b) two-electron oxidation of **3A** and (c) one- and (d) two-electron oxidation of **3B**, (ca. 1 mM) in $CH_2Cl_2$ containing [N$^n$Bu$_4$][BF$_4$] (0.4 M) in an OTE cell at 243 K.

there is cathodic shift in potential from $Zn^{II}$ to $Cu^{II}$ (ca. 60 mV between **2A** and **4A** and ca. 130 mV between **4A** and **4B**). This increase in stability of [**4A/B**]$^+$ relative to [**2A/B**]$^+$ has been observed in related Schiff-base complexes and may be associated with antiferromagnetic coupling between the unpaired electron on the phenoxyl radical and the $d^9$ $Cu^{II}$ center and/or the lower effective nuclear charge of the $Cu^{II}$ center.[10]

**Spectroelectrochemistry of 2A, 2B, 3A, 3B, 4A, and 4B.** The progress of the first one-electron oxidation processes in **2A** and **2B** was followed by UV/vis spectroscopy, which showed the development of absorption bands at about 420 and 780 nm for each oxidation (Table 2, Supporting Information, Figures S1a and S1b). The position of these bands is characteristic of $\pi \rightarrow \pi^*$ transitions of phenoxyl radical ligands, and feature in the electronic spectra of other $Zn^{II}$-phenoxyl radical complexes.[2,12,13,35,68] The observation of isosbestic points at about 275, 343, and 393 nm indicates that the oxidation of **2A** and **2B** produces [**2A**]$^+$ and [**2B**]$^+$, respectively, directly and without the involvement of any detectable intermediates.

The second oxidation processes of **2A** and **2B** are associated with increases in the intensity of the bands at about 420 and 780 nm (Table 2), consistent with the formation of a second coordinated phenoxyl radical ligand.[60] The species formed are unstable over longer timescales, and thus the products generated could not be investigated further.

The chemical nature of the two oxidation processes exhibited by **3A** and **3B** was monitored spectroelectrochemically at 243 K (Table 2, Figure 7). Electrochemical re-reduction to **3A** and **3B** after generation of the singly and doubly oxidized species re-established the original UV/vis profiles showing that the two, one-electron oxidation processes exhibited by **3A** and **3B** are chemically reversible on the timescale of the experiment. The absorption profiles of [**3A**]$^+$ and [**3B**]$^+$ exhibit intense absorptions at about 271, 303, 388, 485, and 668 nm. The bands at about 388 and 485 nm are assigned to LMCT transitions, while the band at about 668 nm may arise from LMCT and/or d → d transitions.[22,35] Unfortunately because of the strong absorbance of both [**3A**]$^+$ and [**3B**]$^+$ around 390 nm, we were unable to determine if characteristic bands associated with the $\pi \rightarrow \pi^*$ transitions of a phenoxyl radical were present in [**3A**]$^+$ and [**3B**]$^+$. Thus, it is not possible to conclude whether the oxidation processes of **3A** and **3B** are ligand- or metal-based through the UV/vis spectroscopic data alone.

The electronic spectra of the products formed by the two-electron oxidation of **3A** and **3B** exhibit absorption bands at 397, 420, 491, and 801 nm for [**3A**]$^{2+}$ and 395, 418, 487, and 799 nm for [**3B**]$^{2+}$ (Table 2, Figure 7). These bands resemble those reported for the bis-phenoxyl radical species obtained by the electrochemical oxidation of [Ni($L^{Py}$)] [$L^{Py}$ = *N,N′,N,N′*-bis[(2-hydroxy-3,5-di-*tert*-butylbenzyl)(2-pyridylmethyl)]-ethylene diamine)] [391 ($\varepsilon$ = 6400), 408 (8240) and 528 nm (3460 $M^{-1}$ $cm^{-1}$)].[34] The intensity and energy of the bands at about 420 and 800 nm in **3A** and **3B**, which are associated with phenoxyl radical $\pi \rightarrow \pi^*$ transitions, are comparable to those formed following the one- and two-electron oxidation of the analogous $Zn^{II}$ complexes, **2A** and **2B**.

UV/vis spectroelectrochemistry demonstrates that the first and second oxidation processes of **4A** and **4B** are chemically reversible under the conditions of the OTE experiment. The absorption profiles of [**4A**]$^+$ and [**4B**]$^+$ reveal intense absorptions at about 386 nm, which are consistent with the phenolate to $Cu^{II}$ LMCT transitions observed in the spectra of **4A** and **4B** (Table 3, Supporting Information, Figure S1 (e) and (f)). The generation of a $Cu^{II}$-phenoxyl radical complex on oxidation of **4A** and **4B** is supported by the appearance of a broad absorption at 720 nm; the other absorption characteristic of the production of a phenoxyl radical at about 410 nm may be masked by the strong band at 386 nm.[10] The absorption spectra of [**4A**]$^{2+}$ and [**4B**]$^{2+}$ exhibit bands at 430, 494, and 764 nm. The energy and intensity of these features are consistent with the $\pi \rightarrow \pi^*$ transitions associated with a bisphenoxyl radical species (Table 3, also see Supporting Information, Figures S1e and S1f).[12,58]

The X-band EPR spectra of electrochemically generated [**2A**]$^+$ and [**2B**]$^+$, in $CH_2Cl_2$ containing $[N^nBu_4][BF_4]$ (0.4 M) at 77 K, are isotropic $S = 1/2$ signals with $g_{iso}$ = 2.004 and 2.005, respectively (Supporting Information, Figure S3). These $g$-values are typical of those for $Zn^{II}$-phenoxyl radical complexes.[2,9,12,68]

The dark brown solutions containing electrochemically generated [**3A**]$^+$ and [**3B**]$^+$ are EPR-active as frozen glasses at 77 K (Figure 8). The EPR spectra of the oxidized species possess rhombic symmetry with anisotropic $g$-tensors ([**3A**]$^+$: $g_{11}$ = 2.413, $g_{22}$ = 2.118, $g_{33}$ = 2.016, and $g_{av}$ = 2.182; [**3B**]$^+$: $g_{11}$ = 2.382, $g_{22}$ = 2.107, $g_{33}$ = 2.023, and $g_{av}$ = 2.171) that are typically associated with metal-centered SOMOs.[22,30,34] The well-defined three-line hyperfine coupling in the $g_{33}$ region that may be simulated by the interaction of a single $^{14}N$ ($I$ = 1)-donor which was assumed to be coordinated to the Ni center ($a_{33}$ = 24.0 G and $a_{33}$ = 23.0 G for [**3A**]$^+$ and [**3B**]$^+$, respectively). These N hyperfine couplings are similar to those reported for the product of the oxidation of NiBDPP [$H_2BDPP$ = 2,6-bis(((*S*)-2-(diphenyl-hydroxymethyl)-1-pyrrolidinyl)-methyl)pyridine, $a_{33}$ = 25 G] which possesses a square pyramidal $N_3O_2$ coordination sphere in which the axial ligand is a pyridine donor.[69]

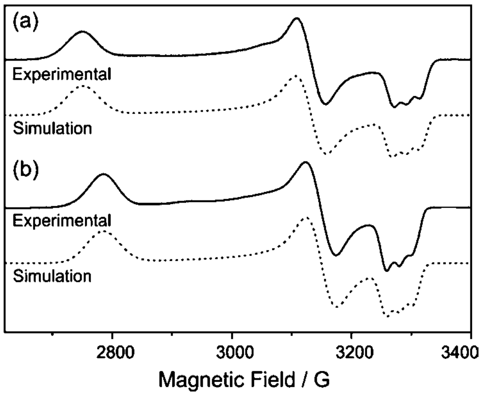

**Figure 8.** Frozen X-band EPR spectra of (a) [**3A**]$^+$ and (b) [**3B**]$^+$ in $CH_2Cl_2$ $[N^nBu_4][BF_4]$ (0.4 M) at 77 K (top), simulated spectra (dotted lines). Spin Hamiltonian parameters for [**3A**]$^+$: $g_{11}$ = 2.413, $g_{22}$ = 2.118, $g_{33}$ = 2.016, $a_{33}$ = 24.0 G, Gaussian linewidths of $W_{11}$ = 54.0, $W_{22}$ = 40.0, and $W_{33}$ = 20.0 G; [**3B**]$^+$: $g_{11}$ = 2.382, $g_{22}$ = 2.107, $g_{33}$ = 2.023, $a_{33}$ = 23.0 G, Gaussian linewidths of $W_{11}$ = 54.0, $W_{22}$ = 40.0, and $W_{33}$ = 19.5 G.

The one-electron oxidation of **3A** to [**3A**]$^+$ was also achieved by chemical oxidation using a stoichiometric quantity of $AgBF_4$ in $CH_2Cl_2$ to produce a dark brown solution containing [**3A**][$BF_4$]. The UV/vis spectrum of [**3A**][$BF_4$] in $CH_2Cl_2$ at 293 K is identical to the corresponding electrochemically generated species (Figure 7a), and remains unchanged for several days. The magnetic susceptibility of a solid sample of [**3A**][$BF_4$] was recorded using a SQUID magnetometer over the temperature range 2−300 K. The magnetic moment ($\mu_{eff}$) of [**3A**][$BF_4$] at 300 K is 1.72 $\mu_B$ ($\chi_T$ = 0.37 $cm^3$ K $mol^{-1}$), consistent with an $S = 1/2$ state (see Supporting Information, Figure S4).

Solutions of $[\mathbf{3A}]^{2+}$ and $[\mathbf{3B}]^{2+}$ in $CH_2Cl_2$ containing $[N^nBu_4][BF_4]$ (0.4 M) are EPR silent at X-band at 293 and 77 K consistent with these species possessing $S = 0$ or 1 (with a large zero-field splitting) ground states, resulting from the magnetic coupling between the coordinated radical ligand(s) and/or the metal center.[34]

Dark green electrochemically-generated $CH_2Cl_2$ solutions of $[\mathbf{4A}]^+$ and $[\mathbf{4B}]^+$ are EPR-silent at 273 and 77 K. This is consistent with $[\mathbf{4A}]^+$ and $[\mathbf{4B}]^+$ possessing $S = 0$ or $S = 1$ ground states that result from the coupling between the $S = 1/2$ $Cu^{II}$ center and a $S = 1/2$ coordinated phenoxyl radical ligand.[2,7,9] The X-band EPR spectra of frozen $[\mathbf{4A}]^{2+}$ and $[\mathbf{4B}]^{2+}$ in $CH_2Cl_2$ $[N^nBu_4][BF_4]$ (0.4 M) solution at 77 K possess isotropic signals ($g_{iso}$ = 2.008 and 2.009 for $[\mathbf{4A}]^{2+}$ and $[\mathbf{4B}]^{2+}$, respectively) consistent with the generation of a second uncoupled phenoxyl radical (see Supporting Information, Figure S5).

**Structural Characterization of [3A][$BF_4$].** Single crystals of [**3A**][$BF_4$] suitable for X-ray crystallography were grown by slow diffusion of pentane into a $CH_2Cl_2$ solution containing the complex. The solid state structure (Figure 9) shows that the distorted square pyramidal coordination sphere of **3A** ($\tau$ = 0.47) rearranges to a distorted trigonal bipyramidal geometry in $[\mathbf{3A}]^+$ ($\tau$ = 0.58). This change in geometry is consistent with the large peak-to-peak separation (ca. 110 mV at 100 mV $s^{-1}$) for the first oxidation process in the cyclic voltammogram of **3A** (see above). This conformational change involves the tertiary amine N-donor, N(3), which is in the axial position in **3A**, moving into the equatorial plane defined by N(3) and the two phenolate O-donors O(1) and O(2) in $[\mathbf{3A}]^+$. The two axial positions in $[\mathbf{3A}]^+$ are occupied by the two imine N-donors, N(1) and N(2). The C−C and C−O distances associated with the two phenolate units within **3A** and $[\mathbf{3A}]^+$ are similar. However, the Ni−O and Ni−N distances in $[\mathbf{3A}]^+$ decrease by about 0.10 Å when compared to the equivalent distances in **3A** (Table 1).

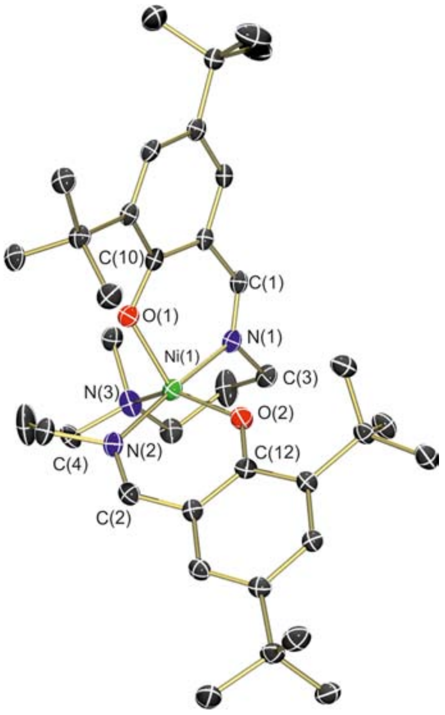

**Figure 9.** View of the cation $[\mathbf{3A}]^+$ in [**3A**][$BF_4$] with displacement ellipsoids at the 50% probability level and H atoms omitted for clarity.

We have performed unrestricted DFT calculations on a model of $[\mathbf{3A}]^+$ to gain insight into the geometric and electronic structure of this center. The selected bond distances and angles for the gas phase geometry optimized structure of $[\mathbf{3A}]^+$ (Table 1) are consistent with a five-coordinate $Ni^{III}$ center ($\tau$ = 0.65) that possesses a greater trigonal prismatic distortion relative to the solid state structure of $[\mathbf{3A}]^+$ derived from X-ray crystallography ($\tau$ = 0.58). The average Ni(1)−N(1/1A) and Ni(1)−O(1/1A) distances are similar in the calculated and experimental structures (Table 1, the average calculated distances are greater by 0.02 and 0.04 Å, respectively) whereas the Ni(1)−N(3) distance is greater by 0.28 Å in the calculated structure. The O(1)−Ni(1)−O(1A) and N(3)−Ni(1)−O(1) angles increase from 115.07(7) to 140.5° and 102.86(8) to 123.8°, respectively, in the calculated structure (Table 1). Thus, although the calculated and experimental structures are broadly similar, in that they possess distorted trigonal prismatic geometries, the principal difference between the calculated and the experimental structures involves the relative distribution of the N(3), O(1), and O(2) donors about the Ni(1) center in the equatorial plane of the approximate trigonal prism. Given the differences in the calculated and experimental structures for $[\mathbf{3A}]^+$ we also undertook unrestricted DFT calculations on a model of **3A** derived from the X-ray crystallographic structure of **3A** to gain insight into these differences. The Ni(1)−N(1/1A), Ni(1)−O(1/1A), and Ni(1)−N(3) distances are similar in the calculated and experimental structures of **3A** (Table 1, the average calculated distances are greater by 0.01, 0.07, and 0.07 Å, respectively), and both geometries exhibit a similar degree of trigonal prismatic distortion ($\tau$ = 0.47 and 0.45 in the experimental and calculated geometries, respectively). Thus, comparisons between the experimental and the geometry optimized structures of **3A** and $[\mathbf{3A}]^+$, together with the differences in experimental geometries for **3A** and [**3A**][$BF_4$], indicate that $[\mathbf{1A}]^{2-}$ can accommodate a range of distorted trigonal bipyramidal geometries.

An analysis of the spin density shows that the unpaired electron in $[\mathbf{3A}]^+$ is localized on Ni(1) (0.495) with contributions from O(1) (0.074), O(2) (0.102) and N(3) (0.067) (Figure 10). The spin density associated with N(3) indicates that coupling to this N-donor leads to the well-defined three-line hyperfine coupling in the $g_{33}$ region (Figure 8). We also note the tendency of the LDA and GGA functionals in these DFT calculations to overestimate the extent of charge delocalization.[70] Thus, the DFT calculations support the X-ray crystallographic, magnetometric and spectroelectrochemical data for [**3A**][$BF_4$] which suggest that the first oxidation of **3A** is metal-based and generates a formal $Ni^{III}$ center.

## ■ CONCLUSIONS

The X-ray crystal structures of [**2A/B**], [**3A/B**], [**4A/B**], and [**3A**][$BF_4$] confirm that $\mathbf{A}^{2-}$ and $\mathbf{B}^{2-}$ can accommodate a range of distorted square pyramidal and trigonal bipyramidal

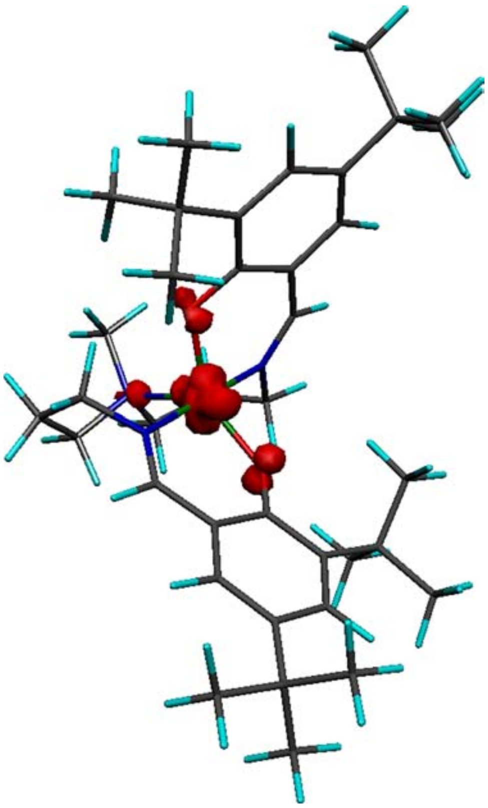

**Figure 10.** Calculated gas-phase geometry optimized structure and spin density for $[\mathbf{3A}]^+$ derived from unrestricted DFT calculations.

geometries characterized by $\tau = 0.37-0.72$. Electrochemical, spectroelectrochemical, and EPR spectroscopic studies confirm that each complex supports two oxidation processes, the first of which may either be predominantly ligand (for [**2A**/**B**] and [**4A**/**B**]) or metal-based (for [**3A**/**B**]). Incorporation of an additional single N-donor into the ligand backbones of $\mathbf{A}^{2-}$ and $\mathbf{B}^{2-}$ is sufficient to switch the redox chemistry in the Ni$^{II}$ complexes from ligand to metal-based without the addition of exogenous or solvent-derived donors. This control of the nature of the redox process within the complex, the plasticity of the ligand in being able to accommodate a range of intermediate coordination geometries, and the isolation of coordinatively unsaturated complexes are being exploited further in the design and synthesis of new catalysts for oxidation reactions.

## ■ ASSOCIATED CONTENT

### Ⓢ Supporting Information

Crystallographic data in CIF format. Further details are given in Table S1 and Figures S1−S5. This material is available free of charge via the Internet at http://pubs.acs.org.

## ■ AUTHOR INFORMATION

### Corresponding Author

*E-mail: j.mcmaster@nottingham.ac.uk (J.M.), m.schroder@nottingham.ac.uk (M.S.). Fax: (+44)115 951 3563. Phone: (+44) 115 951 3498.

### Notes

The authors declare no competing financial interest.

## ■ ACKNOWLEDGMENTS

We thank the EPSRC and the University of Nottingham for support and funding. M.S. gratefully acknowledges receipt of an ERC Advanced Grant.

## ■ REFERENCES

(1) Borman, C. D.; Saysell, C. G.; Sokolowski, A.; Twitchett, M. B.; Wright, C.; Sykes, A. G. *Coord. Chem. Rev.* **1999**, *192*, 771−779.

(2) Jazdzewski, B. A.; Tolman, W. B. *Coord. Chem. Rev.* **2000**, *200*, 633−685.

(3) Whittaker, J. W. *Chem. Rev.* **2003**, *103*, 2347−2363.

(4) Nairn, A. K.; Archibald, S. J.; Bhalla, R.; Gilbert, B. C.; MacLean, E. J.; Teat, S. J.; Walton, P. H. *J. Chem. Soc., Dalton Trans.* **2006**, 172−176.

(5) Rotthaus, O.; Jarjayes, O.; Thomas, F.; Philouze, C.; Del Valle, C. P.; Saint-Aman, E.; Pierre, J. L. *Chem.—Eur. J.* **2006**, *12*, 2293−2302.

(6) Storr, T.; Verma, P.; Pratt, R. C.; Wasinger, E. C.; Shimazaki, Y.; Stack, T. D. P. *J. Am. Chem. Soc.* **2008**, *130*, 15448−15459.

(7) Benisvy, L.; Blake, A. J.; Collison, D.; Davies, E. S.; Garner, C. D.; McInnes, E. J. L.; McMaster, J.; Whittaker, G.; Wilson, C. *Chem. Commun.* **2001**, 1824−1825.

(8) Benisvy, L.; Bill, E.; Blake, A. J.; Collison, D.; Davies, E. S.; Garner, C. D.; Guindy, C. I.; McInnes, E. J. L.; McArdle, G.; McMaster, J.; Wilson, C.; Wolowska, J. *J. Chem. Soc., Dalton Trans.* **2004**, 3647−3653.

(9) Benisvy, L.; Blake, A. J.; Collison, D.; Davies, E. S.; Garner, C. D.; McInnes, E. J. L.; McMaster, J.; Whittaker, G.; Wilson, C. *J. Chem. Soc., Dalton Trans.* **2003**, 1975−1985.

(10) Benisvy, L.; Bill, E.; Blake, A. J.; Collison, D.; Davies, E. S.; Garner, C. D.; McArdle, G.; McInnes, E. J. L.; McMaster, J.; Ross, S. H. K.; Wilson, C. *J. Chem. Soc., Dalton Trans.* **2006**, 258−267.

(11) Itoh, S.; Taki, M.; Fukuzumi, S. *Coord. Chem. Rev.* **2000**, *198*, 3−20.

(12) Halfen, J. A.; Jazdzewski, B. A.; Mahapatra, S.; Berreau, L. M.; Wilkinson, E. C.; Que, L.; Tolman, W. B. *J. Am. Chem. Soc.* **1997**, *119*, 8217−8227.

(13) Bill, E.; Müller, J.; Weyhermüller, T.; Wieghardt, K. *Inorg. Chem.* **1999**, *38*, 5795−5802.

(14) Halfen, J. A.; Young, V. G.; Tolman, W. B. *Angew. Chem., Int. Ed.* **1996**, *35*, 1687−1690.

(15) Itoh, S.; Takayama, S.; Arakawa, R.; Furuta, A.; Komatsu, M.; Ishida, A.; Takamuku, S.; Fukuzumi, S. *Inorg. Chem.* **1997**, *36*, 1407−1416.

(16) Philibert, A.; Thomas, F.; Philouze, C.; Hamman, S.; Saint-Aman, E.; Pierre, J. L. *Chem.—Eur. J.* **2003**, *9*, 3803−3812.

(17) Shimazaki, Y.; Huth, S.; Hirota, S.; Yamauchi, O. *Bull. Chem. Soc. Jpn.* **2000**, *73*, 1187−1195.

(18) Itoh, S.; Taki, M.; Kumei, H.; Takayama, S.; Nagatomo, S.; Kitagawa, T.; Sakurada, N.; Arakawa, R.; Fukuzumi, S. *Inorg. Chem.* **2000**, *39*, 3708−3709.

(19) Thomas, F. *Eur. J. Inorg. Chem.* **2007**, 2379−2404.

(20) Rotthaus, O.; Jarjayes, O.; Del Valle, C. P.; Philouze, C.; Thomas, F. *Chem. Commun.* **2007**, 4462−4464.

(21) Benisvy, L.; Wanke, R.; Guedes da Silva, M. F. C.; Pombeiro, A. J. L. *Eur. J. Inorg. Chem.* **2011**, 2791−2796.

(22) Shimazaki, Y.; Tani, F.; Fukui, K.; Naruta, Y.; Yamauchi, O. *J. Am. Chem. Soc.* **2003**, *125*, 10512−10513.

(23) Arora, H.; Philouze, C.; Jarjayes, O.; Thomas, F. *J. Chem. Soc., Dalton Trans.* **2010**, *39*, 10088−10098.

(24) Rotthaus, O.; Labet, V.; Philouze, C.; Jarjayes, O.; Thomas, F. *Eur. J. Inorg. Chem.* **2008**, 4215−4224.

(25) Rotthaus, O.; Jarjayes, O.; Philouze, C.; Del Valle, C. P.; Thomas, F. *J. Chem. Soc., Dalton Trans.* **2009**, 1792−1800.

(26) Storr, T.; Verma, P.; Shimazaki, Y.; Wasinger, E. C.; Stack, T. D. P. *Chem.—Eur. J.* **2010**, *16*, 8980−8983.

(27) Rotthaus, O.; Jarjayes, O.; Thomas, F.; Philouze, C.; Saint-Aman, E.; Pierre, J. L. *J. Chem. Soc., Dalton Trans.* **2007**, 889−895.

(28) Benisvy, L.; Kannappan, R.; Song, Y. F.; Milikisyants, S.; Huber, M.; Mutikainen, I.; Turpeinen, U.; Gamez, P.; Bernasconi, L.; Baerends, E. J.; Hartl, F.; Reedijk, J. *Eur. J. Inorg. Chem.* **2007**, 637–642.

(29) Freire, C.; de Castro, B. *Polyhedron* **1998**, *17*, 4227–4235.

(30) Freire, C.; de Castro, B. *J. Chem. Soc., Dalton Trans.* **1998**, 1491–1497.

(31) Glaser, T.; Heidemeler, M.; Frohlich, R.; Hildebrandt, P.; Bothe, E.; Bill, E. *Inorg. Chem.* **2005**, *44*, 5467–5482.

(32) Shimazaki, Y.; Yajima, T.; Tani, F.; Karasawa, S.; Fukui, K.; Naruta, Y.; Yamauchi, O. *J. Am. Chem. Soc.* **2007**, *129*, 2559–2568.

(33) Storr, T.; Wasinger, E. C.; Pratt, R. C.; Stack, T. D. P. *Angew. Chem., Int. Ed.* **2007**, *46*, 5198–5201.

(34) Rotthaus, O.; Thomas, F.; Jarjayes, O.; Philouze, C.; Saint-Aman, E.; Pierre, J. L. *Chem.—Eur. J.* **2006**, *12*, 6953–6962.

(35) Parker, D.; Davies, E. S.; Wilson, C.; McMaster, J. *Inorg. Chim. Acta* **2007**, *360*, 203–211.

(36) Müller, J.; Kikuchi, A.; Bill, E.; Weyhermüller, T.; Hildebrandt, P.; Ould-Moussa, L.; Wieghardt, K. *Inorg. Chim. Acta* **2000**, *297*, 265–277.

(37) Bencini, A.; Carbonera, C.; Dei, A.; Vaz, M. G. F. *J. Chem. Soc., Dalton Trans.* **2003**, 1701–1706.

(38) Sheldrick, G. M. *Acta Crystallogr., Sect. A* **2008**, *64*, 112–122.

(39) Altomare, A.; Cascarano, G.; Giacovazzo, C.; Guagliardi, A. *J. Appl. Crystallogr.* **1993**, *26*, 343–350.

(40) Allen, F. H.; Johnson, O.; Shields, G. P.; Smith, B. R.; Towler, M. *J. Appl. Crystallogr.* **2004**, *37*, 335–338.

(41) International Union of Crystallography, http:/checkcif.iucr.org

(42) Guerra, C. F.; Snijders, J. G.; Te Velde, G.; Baerends, E. J. *Theor. Chem. Acc.* **1998**, *99*, 391–403.

(43) Te Velde, G.; Bickelhaupt, F. M.; Baerends, E. J.; Guerra, C. F.; Van Gisbergen, S. J. A.; Snijders, J. G.; Ziegler, T. *J. Comput. Chem.* **2001**, *22*, 931–967.

(44) Vosko, S. H.; Wilk, L.; Nusair, M. *Can. J. Phys.* **1980**, *58*, 1200–1211.

(45) Becke, A. D. *Phys. Rev. A.* **1988**, *38*, 3098–3100.

(46) Perdew, J. P. *Phys. Rev. B.* **1986**, 8822–8824.

(47) Portmann, S.; Luthi, H. P. *Chimia* **2000**, *54*, 766–770.

(48) Zhu, D.; Su, Z.; Mu, Z.; Qiu, Y.; Wang, Y. *J. Coord. Chem.* **2006**, *59*, 409–419.

(49) Tai, X. S.; Feng, Y. M.; Zhang, H. X. *Acta. Crystallogr., Sect. E.* **2008**, *64*, M502–U641.

(50) Freyberg, D. P.; Mockler, G. M.; Sinn, E. *J. Chem. Soc., Dalton Trans.* **1976**, 447–454.

(51) Addison, A. W.; Rao, T. N.; Reedijk, J.; Vanrijn, J.; Verschoor, G. C. *J. Chem. Soc., Dalton Trans.* **1984**, 1349–1356.

(52) Seleborg, M.; Holt, S. L.; Post, B. *Inorg. Chem.* **1971**, *10*, 1501–1502.

(53) Orioli, P. L.; Divaira, M.; Sacconi, L. *Chem. Commun.* **1966**, 300–301.

(54) Healy, P. C.; Mockler, G. M.; Freyberg, D. P.; Sinn, E. *J. Chem. Soc., Dalton Trans.* **1975**, 691–698.

(55) Divaira, M.; Sacconi, L.; Orioli, P. L. *Inorg. Chem.* **1971**, *10*, 553–554.

(56) Amirnasr, M.; Schenk, K. J.; Meghdadi, S.; Morshedi, M. *Polyhedron* **2006**, *25*, 671–677.

(57) Yilmaz, V. T.; Degirmencioglu, I.; Andac, O.; Karabocek, S.; Slawin, A. M. Z. *J. Mol. Struct.* **2003**, *654*, 125–129.

(58) Sokolowski, A.; Leutbecher, H.; Weyhermüller, T.; Schnepf, R.; Both, E.; Bill, E.; Hildebrandt, P.; Wieghardt, K. *J. Biol. Inorg. Chem.* **1997**, *2*, 444–453.

(59) Kumar, D. N.; Garg, B. S. *Spectrochim. Acta, Part A* **2006**, *64*, 141–147.

(60) Orio, M.; Philouze, C.; Jarjayes, O.; Neese, F.; Thomas, F. *Inorg. Chem.* **2010**, *49*, 646–658.

(61) Downing, R. S.; Urbach, F. L. *J. Am. Chem. Soc.* **1969**, *91*, 5977–5978.

(62) Amundsen, A. R.; Whelan, J.; Bosnich, B. *J. Am. Chem. Soc.* **1977**, *99*, 6730–6739.

(63) Kasumov, V. T.; Koksal, F. *Spectrochim. Acta, Part A* **2004**, *60*, 31–39.

(64) Collison, D.; Helliwell, M.; Jones, V. M.; Mabbs, F. E.; McInnes, E. J. L.; Riedi, P. C.; Smith, G. M.; Pritchard, R. G.; Cross, W. I. *J. Chem. Soc., Faraday Trans.* **1998**, *94*, 3019–3025.

(65) Krzystek, J.; Park, J. H.; Meisel, M. W.; Hitchman, M. A.; Stratemeier, H.; Brunel, L. C.; Telser, J. *Inorg. Chem.* **2002**, *41*, 4478–4487.

(66) Rogez, G.; Rebilly, J. N.; Barra, A. L.; Sorace, L.; Blondin, G.; Kirchner, N.; Duran, M.; van Slageren, J.; Parsons, S.; Ricard, L.; Marvilliers, A.; Mallah, T. *Angew. Chem., Int. Ed.* **2005**, *44*, 1876–1879.

(67) Zanello, P. *Inorganic Electrochemistry, Theory, Practice and Application*; Royal Society of Chemistry: Cambridge, U.K., 2003.

(68) Sokolowski, A.; Müller, J.; Weyhermüller, T.; Schnepf, R.; Hildebrandt, P.; Hildenbrand, K.; Bothe, E.; Wieghardt, K. *J. Am. Chem. Soc.* **1997**, *119*, 8889–8900.

(69) Lee, W.-Z.; Chiang, C.-W.; Lin, T.-H.; Kuo, T.-S. *Chem.—Eur. J.* **2012**, *18*, 50–53.

(70) Cramer, C. J.; Truhlar, D. G. *Phys. Chem. Chem. Phys.* **2009**, *11*, 10757–10816.